



## Reconstructed anti-poisoning surface for enhanced electrochemical CO<sub>2</sub> reduction on Cu-incorporated ZnO

Jinxian Feng <sup>a</sup>, Junyan Li <sup>b</sup>, Lulu Qiao <sup>a</sup>, Dong Liu <sup>c</sup>, Pengfei Zhou <sup>a</sup>, Jun Ni <sup>d</sup>, Hui Pan <sup>a,e,\*</sup>

<sup>a</sup> Institute of Applied Physics and Materials Engineering, University of Macau, Macao Special Administrative Region of China

<sup>b</sup> State Key Laboratory of Quality Research in Chinese Medicine, University of Macau, Macao Special Administrative Region of China

<sup>c</sup> College of Materials Science and Engineering, Shenzhen University, Shenzhen 518071, China

<sup>d</sup> Institute of Industrial Catalysis, Zhejiang University of Technology, Hangzhou 310014, China

<sup>e</sup> Department of Physics and Chemistry, Faculty of Science and Technology, University of Macau, Macao Special Administrative Region of China



### ARTICLE INFO

#### Keywords:

CO<sub>2</sub> reduction  
Surface anti-poisoning  
Zn oxide  
Cu-incorporation  
Electrocatalyst

### ABSTRACT

Zn-based materials are regarded as a family of promising electrocatalysts for electrochemical CO<sub>2</sub> reduction reaction (e-CO<sub>2</sub>RR), especially for the CO<sub>2</sub>-to-CO conversion. However, their electrocatalytic performances should be improved and the conversion mechanism needs to be further studied. In this work, we fabricate Cu-incorporated ZnO (Cu<sub>25</sub>Zn-A) on Zn plate for e-CO<sub>2</sub>RR catalyst by a facile annealing method. We find that Cu<sub>25</sub>Zn-A achieves a high CO Faraday efficiency > 90% with a CO yield rate of 0.49 mmol cm<sup>-2</sup> h<sup>-1</sup>. The improved catalytic activity on Cu<sub>25</sub>Zn-A is mainly attributed to the Cu steps on the reconstructed surface in the reaction: (1) that weakens the OH/CO<sub>3</sub><sup>2-</sup> adsorption, leading to the anti-poisoning surface by preventing the formation of Zn hydroxide/carbonates; and (2) that enhances the adsorption/activation of reactants and stabilizes the intermediates. Additionally, the density of defects in Zn oxide is increased by the Cu-incorporation, resulting in improved deoxygenation step. Our findings may provide insightful understanding on the mechanism and guide the design of novel electrocatalyst for effective CO<sub>2</sub> reduction.

### 1. Introduction

With the development of human society, fossil fuels are greatly consumed, leading to ever-increasing CO<sub>2</sub> emission and shortage of energy [1,2]. The CO<sub>2</sub> concentration in the atmosphere is going to be over 400 ppm and predicted to be 560 ppm by 2030, which shall result in serious environmental crisis [3,4]. Therefore, various methods have been developed to reduce the CO<sub>2</sub> amount in the atmosphere. Among all them, electrochemical CO<sub>2</sub> reduction reaction in aqueous media (e-CO<sub>2</sub>RR) is one of the most promising strategies because it can not only convert CO<sub>2</sub> into chemical products in ambient condition, but also store and control the unstable sustainable power sources powered by renewable electricity [5]. So far, various chemicals can be generated by e-CO<sub>2</sub>RR, such as formate (HCOOH) [6,7], alcohols [8,9], carbon monoxide (CO) [10,11], methane (CH<sub>4</sub>) [12,13], and ethylene (C<sub>2</sub>H<sub>4</sub>) [14,15]. Among these products, CO as an energy-containing molecule can be used for fuels and is one of most important feedstocks in medical industry, light industry, metallurgy and so on [16,17]. Therefore, great effort has been made to develop electrocatalysts for the reduction of CO<sub>2</sub>.

to CO efficiently [18,19]. Many cost-effective elements have been investigated for the purpose. Among them, zinc (Zn) is promising because of its high CO Faraday efficiency (FE) and low FE for hydrogen production [20,21]. Recently, it was reported that the CO FE of Zn could be significantly enhanced by incorporating other elements, such as Mo [22], Cu[23] and Ag [24]. Cu and Zn have been confirmed to be an efficient electrocatalytic couple for the CO generation in e-CO<sub>2</sub>RR [25, 26]. Although extensive studies have been done to improve the activity of Zn-based electrocatalyst with Cu, the mechanism on the improvement still remains unclear.

It is well known that the surface of electrocatalyst shall undergo reconstruction during the reaction. By using KHCO<sub>3</sub> as electrolyte in e-CO<sub>2</sub>RR, ZnO may react with OH<sup>-</sup> and CO<sub>3</sub><sup>2-</sup>, leading to Zn(OH)<sub>2</sub> and Zn<sub>5</sub>(CO<sub>3</sub>)<sub>2</sub>(OH)<sub>6</sub> on the surface [27]. They not only cover the active sites on the surface, but also reduce the electronic conductivity, resulting in the surface poisoning and reduced activity. Therefore, the surface of electrocatalyst should be well-designed. Unfortunately, there is little attention on preventing the surface from poisoning in e-CO<sub>2</sub>RR, and the mechanism has not been revealed. It is thus essential to study

\* Correspondence to: Institute of Applied Physics and Materials Engineering, University of Macau, Macao S. A. R., China. +853-88222454 (fax).  
E-mail address: [huipan@um.edu.mo](mailto:huipan@um.edu.mo) (H. Pan).

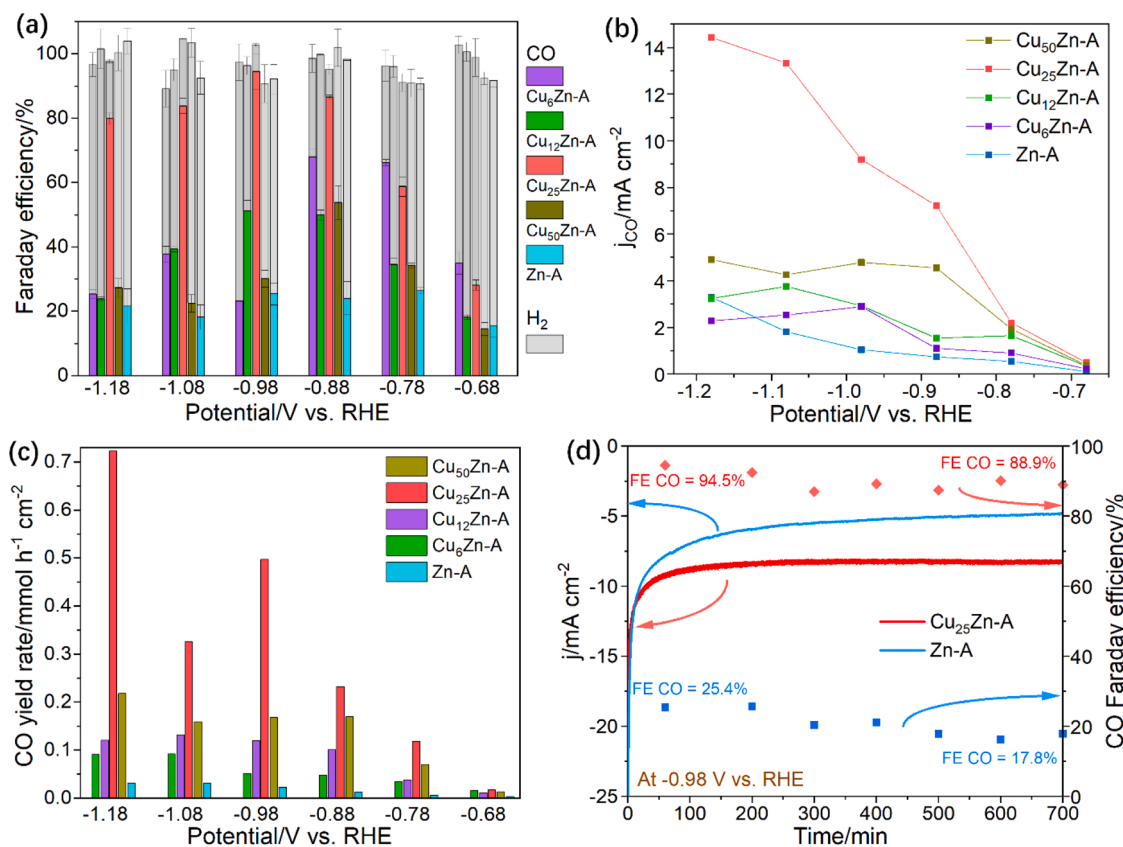


**Fig. 1.** (a) FEs of CO and H<sub>2</sub>, (b) CO partial current densities and (c) CO yield rates of Zn-A, Cu<sub>6</sub>Zn-A, Cu<sub>12</sub>Zn-A, Cu<sub>25</sub>Zn-A and Cu<sub>50</sub>Zn-A at different potentials. (d) Potentiostatic curves of Zn-A and Cu<sub>25</sub>Zn-A at -0.98 V vs. RHE.

surface-modified ZnO for selective CO generation in e-CO<sub>2</sub>RR and offer a model for the deep understanding on the surface anti-poisoning.

In this work, we fabricate Cu-incorporated Zn oxide (Cu<sub>25</sub>Zn-A) on Zn plate as electrocatalyst for e-CO<sub>2</sub>RR by a combined surface-element exchange and annealing method. A FE for CO of > 90%, a CO partial current density of 9.19 mA cm<sup>-2</sup>, and a CO yield rate of 0.49 mmol cm<sup>-2</sup> h<sup>-1</sup> are achieved on Cu<sub>25</sub>Zn-A at the potential of -0.98 V (vs. RHE, if there is no other statement), which are much higher than those on annealed Zn plate (Zn-A) and other electrocatalysts with similar chemical compositions. Most importantly, we find that the metallic phase with Cu steps is in-situ generated on Cu<sub>25</sub>Zn-A, resulting in the surface anti-poisoning by preventing Zn(OH)<sub>2</sub> and Zn<sub>5</sub>(CO<sub>3</sub>)<sub>2</sub>(OH)<sub>6</sub> from forming, which can inhibit the OH<sup>-</sup>/CO<sub>3</sub><sup>2-</sup> adsorption and enhance the proton concentration. Meanwhile, the Cu steps could improve the adsorption/activation of reactants and stabilize the intermediates in e-CO<sub>2</sub>RR. Additionally, the Cu-incorporation improves the amount of defects, benefiting the deoxygenation steps as well.

## 2. Experimental method

### 2.1. Chemicals and reagents

Copper (II) dichloride hexahydrate (CuCl<sub>2</sub>·6 H<sub>2</sub>O, >99%), sodium hydroxide (NaOH, >97%), hydrochloric acid (HCl, AR, 32%), potassium bicarbonate (KHCO<sub>3</sub>, AR, >99%), potassium thiocyanate (KSCN, AR) and ethanol were purchased from Aladdin, Co. Ltd. Zn and Cu plate (purity >99.9%, 0.1 mm in thickness) was purchased from Wanda Scientific Materials, Xingtai, Hebei. All chemicals were utilized as received without any treatment. Deionized (DI) water was supplied by a Barnstead Nanopure water system (resistivity: 18.3 MΩ/cm) and used for the preparation of all aqueous solutions.

### 2.2. Electrocatalyst fabrication

A piece of Zn plate (Zn, 4 cm × 2 cm) was firstly soaked in 1 M NaOH solution for 20 min, and then washed by DI water to remove residual NaOH. The treated Zn plate was then immersed in 1 M HCl aqueous solution to remove the surface oxide and washed by DI water. After that, the Zn plate was immersed in 10 mL CuCl<sub>2</sub> solution for 15 min, then taken out and heated in an oven at 60 °C for 1 h. The sample was then placed in a porcelain boat and annealed at 400 °C in air for 4 h by using tube-oven (Ke Jing Co. Ltd. Hefei, OTF-1200X). To obtain samples with different Cu contents, the concentration of CuCl<sub>2</sub> in solution was controlled.

### 2.3. Materials characterizations

The morphology and chemical composition were determined by scanning electron microscope (SEM) (ZEISS-Merlin) and transmission electron microscope (TEM) (JEM-F200) with energy-dispersive X-ray spectroscopy (EDS). Powder X-ray diffraction (XRD) measurements were conducted on a Rigaku rotating anode diffractometer with a mono chromated Cu K $\alpha$  X-ray source. Raman spectra were recorded by a confocal laser Raman system using a 532 nm laser as excitation wavelength, with an acquisition time of 15 s. X-ray photoelectron spectroscopy (XPS) spectra were collected on a Thermo Fisher Scientific Theta Probe with Mg K $\alpha$  ( $h\nu = 1253.6$  eV) as the excitation source. Inductively coupled optical emission spectrometry (ICP-OES) measurement was conducted to measure the concentrations of elements in the sample (iCAP Qs ICP-MS, Thermo scientific) by dissolving it in 5% nitric acid. The Cu content of Cu<sub>25</sub>Zn-A is 0.1745 mg/cm<sup>2</sup>.

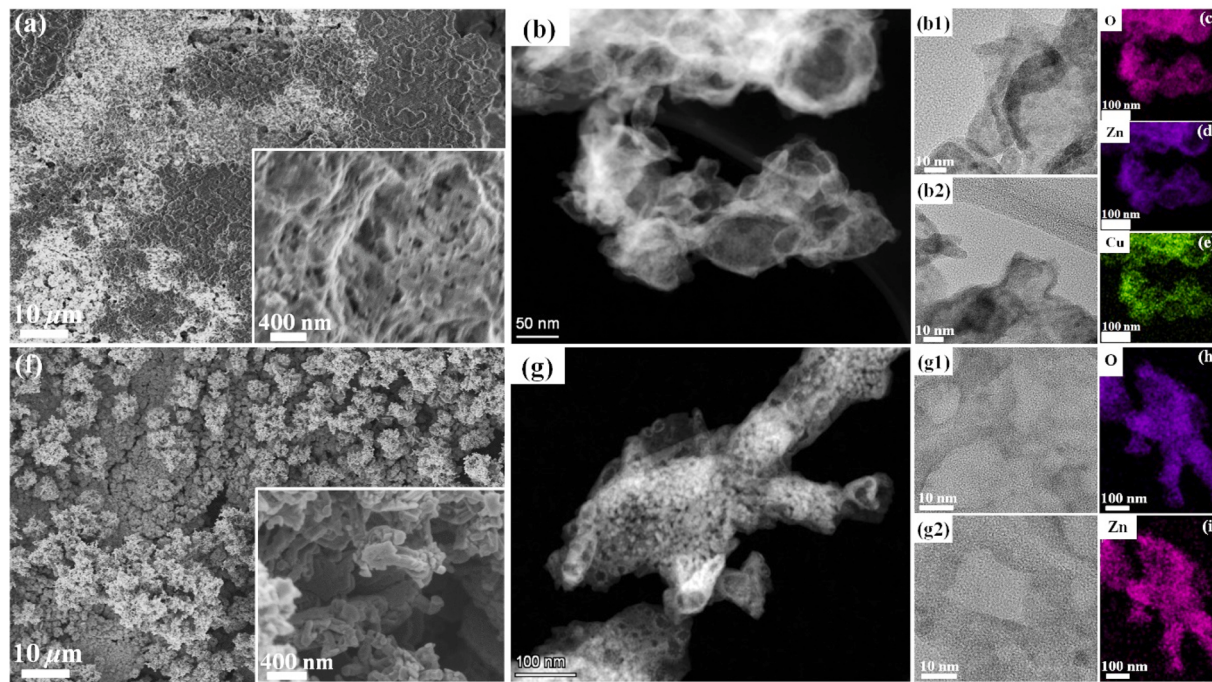


**Fig. 2.** Cu<sub>25</sub>Zn-A: (a) SEM images, (b) HRTEM-HAADF images, (b1-b2) TEM images, and (c-e) TEM-EDS mappings. Zn-A: (f) SEM images, (g) HAADF-STEM images, (g1-g2) TEM images, and (h-i) TEM-EDS mappings of Zn and O of Zn-A. The insets in (a) and (f) show the fine views.

#### 2.4. Electrochemical test

The electrochemical tests were conducted on an electrochemical workstation (CHI 760D) with a standard three-electrode cell at room temperature. 0.5 M KHCO<sub>3</sub> saturated with CO<sub>2</sub> was used as electrolyte. The as-prepared sample, a Ti mesh with Ru-Ir oxide coating, and an Ag/AgCl (3 M KCl) electrode were used as the working, counter and reference electrodes, respectively. Potential was converted to the reversible hydrogen electrode (RHE) via the Nernst equation (E vs. RHE = E vs. Ag/AgCl + 0.0591 × pH + 0.198 V). The electrochemical impedance spectroscopy (EIS) was measured in the frequency range of 0.01–10<sup>5</sup> Hz with an amplitude of 10 mV. The EIS raw data were fitted by ZView software.

#### 2.5. Product Analysis

The FE of CO and gaseous organic products were measured by gas chromatography (GC) (7890B, Agilent Technologies) with a flame-ionized detector (FID), and the hydrogen gas was measured by GC with thermal conductivity detector (TCD). The liquid products were analyzed by <sup>1</sup>H nuclear magnetron resonance (<sup>1</sup>H NMR) (Bruker, 600 MHz). The formate (0.167 M) + methanol (0.164 M) + ethanol (0.114 M) in CO<sub>2</sub>-saturated 0.5 M KHCO<sub>3</sub> was utilized as standard specimen for qualitative analysis. For each electrocatalyst, the electrolyte after the CO<sub>2</sub> reduction at different potentials were mixed, and their <sup>1</sup>H NMR spectra were measured. There is no liquid product if a mixed sample does not show the <sup>1</sup>H NMR organic characteristic peak.

#### 2.6. In-situ Raman analysis

In-situ Raman spectrum was measured by using Teflon in-situ Raman cell. The Raman excitation wavelength is 532 nm, the power ratio is 100% and the acquisition time is 20 s. The current intensities were directly controlled by an electrochemical workstation (CHI 760E).

### 3. Results and Discussions

#### 3.1. Electrochemical Performances

Electrochemical measurements for e-CO<sub>2</sub>RR were conducted firstly. The experimental methods were described in supporting information. The test was held in CO<sub>2</sub>-saturated 0.5 M KHCO<sub>3</sub> (pH=7.2). The gaseous products were examined by GC. The highest CO FE of Cu<sub>25</sub>Zn-A is 94.5% at –0.98 V in average (Fig. 1a). The CO partial current density and CO yield rate of Cu<sub>25</sub>Zn-A are 9.19 mA cm<sup>-2</sup> and 0.49 mmol h<sup>-1</sup> cm<sup>-2</sup> at –0.98 V, and 14.4 mA cm<sup>-2</sup> and 0.72 mmol h<sup>-1</sup> cm<sup>-2</sup> at –1.18 V, respectively. For the gaseous products of Cu<sub>25</sub>Zn-A in e-CO<sub>2</sub>RR, only CO can be detected (Figure S1a). Liquid products were analyzed by <sup>1</sup>H NMR using heavy water as solvent. For Cu<sub>25</sub>Zn-A, the <sup>1</sup>H NMR spectra of mixed electrolytes after the reduction at different potentials only show the characteristic peaks of water, suggesting negligible liquid products (Figure S1b). The GC and <sup>1</sup>H NMR results imply that Cu<sub>25</sub>Zn-A has high selectivity toward CO. For the Zn plate annealed at 400 °C (Zn-A), only CO can be detected and liquid products are negligible too (Figure S2). The highest CO FE for Zn-A is 25.4% at –0.98 V (Fig. 1a). The CO partial current density and CO yield rate of Zn-A are 1.04 mA cm<sup>-2</sup> and 0.023 mmol h<sup>-1</sup> cm<sup>-2</sup> at –0.98 V, and 3.30 mA cm<sup>-2</sup> and 0.063 mmol h<sup>-1</sup> cm<sup>-2</sup> at –1.18 V, respectively, lower than those of Cu<sub>25</sub>Zn-A (Fig. 1b-c). Additionally, Cu<sub>25</sub>Zn-A shows smaller FE for hydrogen generation than Zn-A at the same potential (Fig. 1a). All those results suggest that Cu<sub>25</sub>Zn-A is much more catalytically active for the CO<sub>2</sub>-to-CO conversion than Zn-A.

To investigate the effect of Cu loading on the catalytic performance in e-CO<sub>2</sub>RR, the Cu-Zn electrocatalysts with different Cu contents were studied too. The CuCl<sub>2</sub> solutions with different concentrations (50, 25, 12 and 6 mM) were utilized as feedstock to load Cu onto the Zn plate (denoted as Cu<sub>50</sub>Zn-A, Cu<sub>12</sub>Zn-A and Cu<sub>6</sub>Zn-A, respectively). The Cu content on the surface increases as the CuCl<sub>2</sub> concentration increases in the feedstock (Figures S3 & S4). At the same time, the GC curves of Cu<sub>50</sub>Zn-A, Cu<sub>12</sub>Zn-A and Cu<sub>6</sub>Zn-A measured at different potentials also confirm that only CO can be detected (Figures S5a, 6a & 7a). Similarly, the <sup>1</sup>H NMR spectra of the mixed electrolytes after the electrochemical

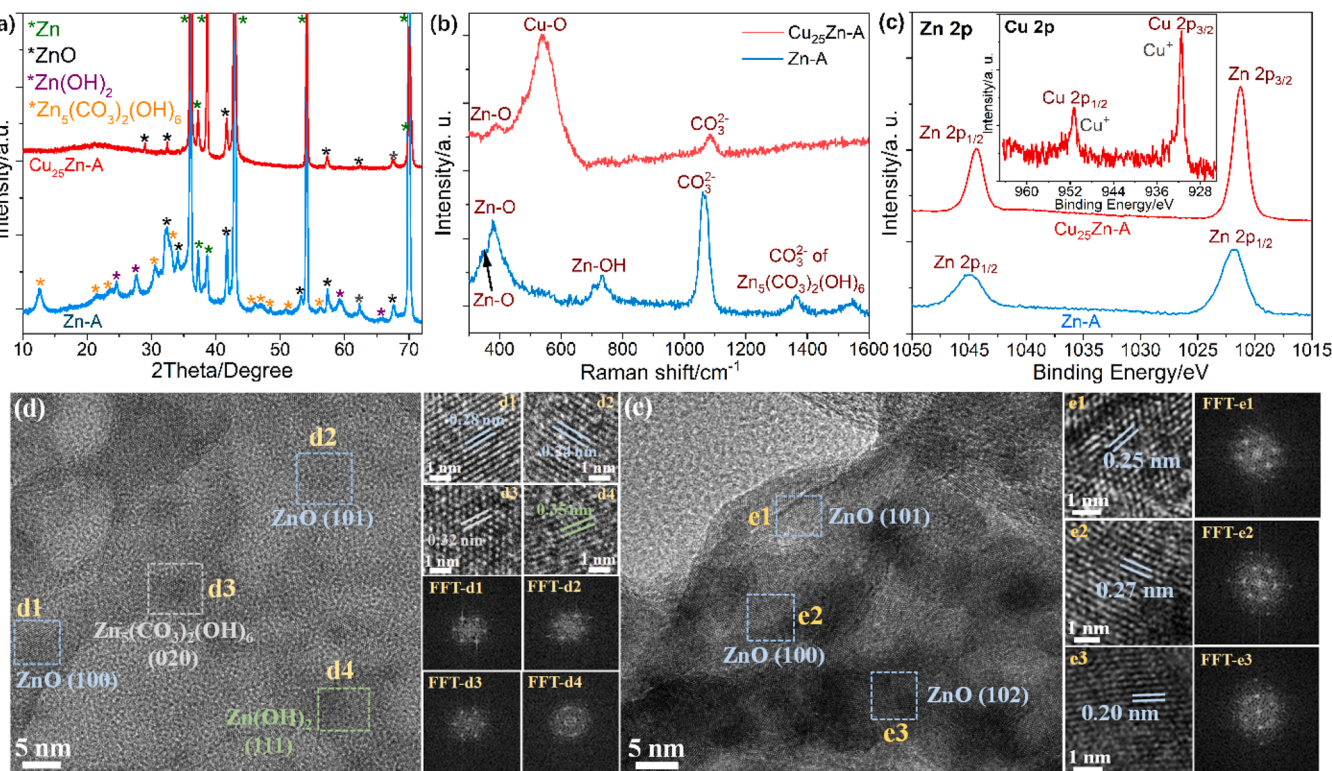


**Fig. 3.** Characterizations of Zn-A and Cu<sub>25</sub>Zn-A after the stability tests: (a) XRD patterns, (b) Raman spectra, (c) Zn 2p XPS spectra (Inset: Cu 2p XPS spectrum of Cu<sub>25</sub>Zn-A), HRTEM images, crystal lattice in high magnification and corresponding FFT patterns: (d) Zn-A, (e) Cu<sub>25</sub>Zn-A.

tests for Cu<sub>6</sub>Zn-A, Cu<sub>12</sub>Zn-A and Cu<sub>50</sub>Zn-A at different potentials show negligible liquid products (Figures S5b, 6b & 7b). Clearly, we see that Cu<sub>25</sub>Zn-A shows much higher CO FE, CO partial current density, and CO yield rate, and lower FE for H<sub>2</sub> than Cu<sub>50</sub>Zn-A, Cu<sub>12</sub>Zn-A, and Cu<sub>6</sub>Zn-A (Fig. 1a-c), suggesting that the Cu content of Cu<sub>25</sub>Zn-A is optimal. Additionally, the 700-minute galvanostatic measurements at -0.98 V show that Cu<sub>25</sub>Zn-A has larger current density than Zn-A (Fig. 1d). Meanwhile, the CO FE of Cu<sub>25</sub>Zn-A are much higher than that of Zn-A in the 700-minute potentiostatic test, indicating Cu<sub>25</sub>Zn-A is highly stable (Fig. 1d). Furthermore, the EDS spectra of Cu<sub>25</sub>Zn-A after the stability tests for 60 (Figure S3c) and 700 min in e-CO<sub>2</sub>RR (Figure S8) show that the Cu content has negligible loss, further confirming its long-term stability. Additionally, Cu<sub>25</sub>Zn-A shows low FE CO and partial current density of CO when 5 mM KSCN + 0.5 M KHCO<sub>3</sub> is used as electrolyte, suggesting Cu plays the dominant role in the CO<sub>2</sub>-to-CO conversion (Figure S9). Importantly, Cu<sub>25</sub>Zn-A shows higher CO FE and yield rates than most of electrocatalysts with similar composition (Table S1).

### 3.2. Physical and chemical structure characterizations

The surface morphologies of Cu<sub>25</sub>Zn-A and Zn-A after the 700-minute test at -0.98 V in e-CO<sub>2</sub>RR (the following experiments were based on the samples after the 700-minute test in e-CO<sub>2</sub>RR at -0.98 V if there is no other statement) were characterized by SEM and TEM. The SEM images show that the surface of Cu<sub>25</sub>Zn-A is a sponge-like structure, which is consisted of skeletons with a width of ~150 nm, and numerous nanopores with a diameter of ~50 nm among the skeletons (Fig. 2a), leading to large surface area and open structure. For Zn-A, the surface is composed of various aggregated nano granules with a size of ~100 nm (Fig. 2f). The high angle annular dark-field scanning transmission electron microscopy (HAADF-STEM) and TEM were utilized to study the morphologies and compositions of Cu<sub>25</sub>Zn-A and Zn-A further. The HAADF-STEM and TEM images confirm the sponge-like surface of Cu<sub>25</sub>Zn-A, where many wrinkles locate on the skeletons (Figs. 2b, b1 &

b2). The cross-linked nanogranules appear on Zn-A, where various nanosized holes are among the skeletons (Figs. 2g, g1 & g2). The TEM-EDS mappings show that the Cu, Zn and O elements are evenly distributed in Cu<sub>25</sub>Zn-A (Fig. 2c-e), and only Zn and O are observed in Zn-A (Fig. 2h-i).

The XRD, Raman spectroscopy and XPS were utilized to study the physical and chemical properties of electrocatalysts after the 700-minute tests. The XRD patterns of Cu<sub>25</sub>Zn-A and Zn-A show the characteristic peaks of Zn (JCPDS #04-0831) and ZnO (JCPDS #36-1451) (Fig. 3a, S10). For Cu<sub>25</sub>Zn-A, there is no diffraction peak for Cu or its compounds, suggesting that Cu is incorporated into ZnO (Fig. 3a). Importantly, the XRD patterns show that Zn(OH)<sub>2</sub> and Zn<sub>5</sub>(CO<sub>3</sub>)<sub>2</sub>(OH)<sub>6</sub> are present in Zn-A, which are not observable in Cu<sub>25</sub>Zn-A after the stability test, indicating that the Cu-incorporation can prevent the ZnO surface from poisoning in e-CO<sub>2</sub>RR (Fig. 3a).

The Raman spectrum of Cu<sub>25</sub>Zn-A shows two characteristic peaks within 300-1000 cm<sup>-1</sup>: one for Zn-O and the other one for Cu-O. Zn-A has three Raman characteristic peaks within 300-1000 cm<sup>-1</sup>: two for Zn-O and one for Zn-OH (Fig. 3b) [28], suggesting the existence of oxides on both electrocatalysts. The Raman spectra of Cu<sub>25</sub>Zn-A and Zn-A after the stability tests within 1000-2000 cm<sup>-1</sup> were utilized to study the bonding states of poisoning species (especially CO<sub>3</sub><sup>2-</sup>). We can see that the characteristic peaks for CO<sub>3</sub><sup>2-</sup> and O-H of water molecules are present in the Raman spectrum of Cu<sub>25</sub>Zn-A [7], which should be attributed to the ions and moisture of residual electrolyte on the sample surface (Fig. 3b) [29]. For Zn-A, the characteristic peaks for CO<sub>3</sub><sup>2-</sup> (~1380 cm<sup>-1</sup> and 1580 cm<sup>-1</sup>) can be observed additionally [29,30], implying the existence of Zn<sub>5</sub>(CO<sub>3</sub>)<sub>2</sub>(OH)<sub>6</sub> on its surface further. At the same time, Zn-A shows much stronger peaks for Zn-OH and CO<sub>3</sub><sup>2-</sup> than Cu<sub>25</sub>Zn-A, indicating that there are abundant CO<sub>3</sub><sup>2-</sup> and OH<sup>-</sup> on its surface. Meanwhile, the CO<sub>3</sub><sup>2-</sup> peak for Zn-A is red-shift by ~30 cm<sup>-1</sup> compared with that for Cu<sub>25</sub>Zn-A, indicating that CO<sub>3</sub><sup>2-</sup> is more strongly adsorbed on the surface of Zn-A than that on Cu<sub>25</sub>Zn-A (Fig. 3b) [31,32]. Additionally, in-situ Raman spectra of Zn-A show the peaks of Zn-OH and CO<sub>3</sub><sup>2-</sup> for

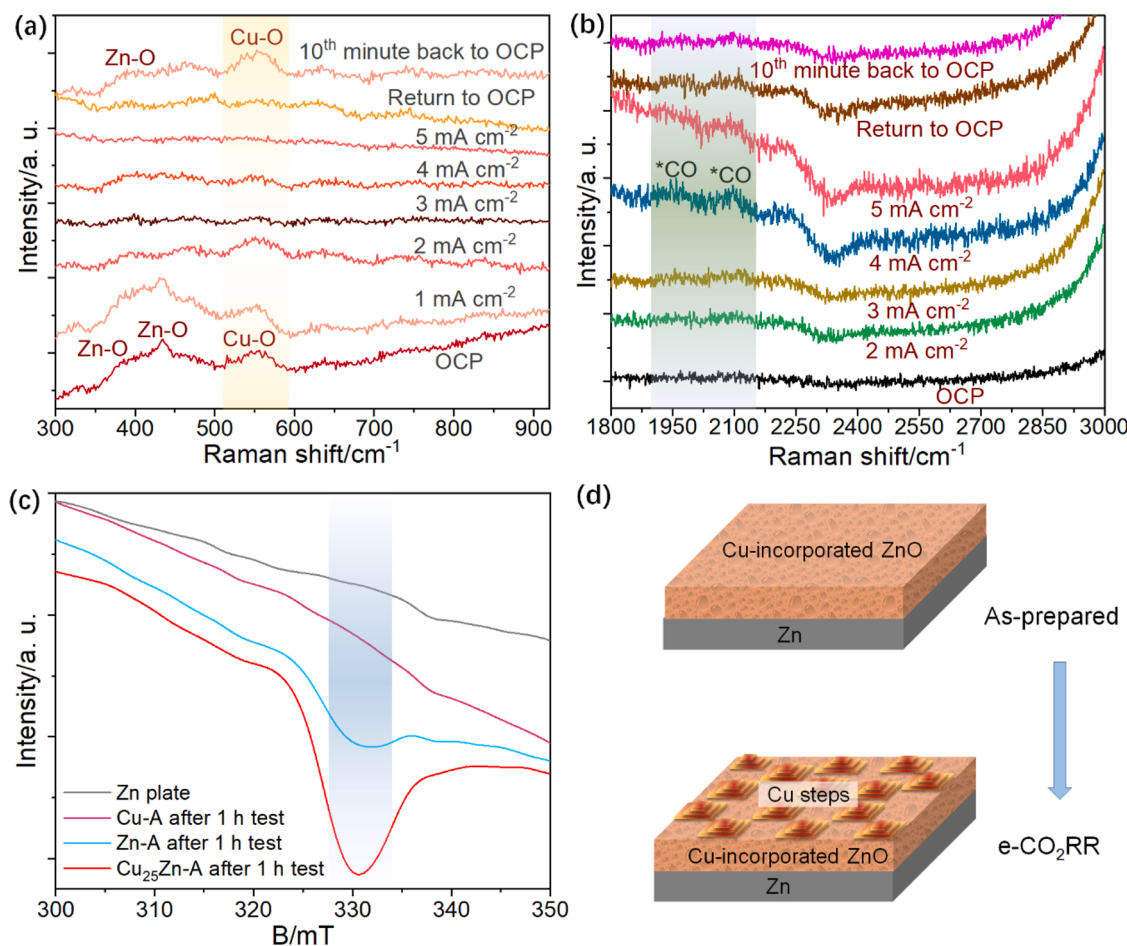


**Fig. 4.** In-situ Raman spectra for of Cu<sub>25</sub>Zn-A in a range of: (a) 300–900 cm<sup>-1</sup> and (b) 1800–3000 cm<sup>-1</sup>. (c) ESR spectra of Zn plate, and quasi in-situ ESR spectra of Cu-A, Zn-A and Cu<sub>25</sub>Zn-A at 5<sup>th</sup> minute after the 1 h e-CO<sub>2</sub>RR test. (d) Scheme for the surface evolution of Cu<sub>25</sub>Zn-A.

Zn<sub>5</sub>(CO<sub>3</sub>)<sub>2</sub>(OH)<sub>6</sub> when the current is over 3 mA cm<sup>-2</sup>, which keep existed after back to open circuit potential (OCP) for 10 min (Figure S11), suggesting that Zn(OH)<sub>2</sub> and Zn<sub>5</sub>(CO<sub>3</sub>)<sub>2</sub>(OH)<sub>6</sub> are formed during the CO<sub>2</sub>RR reaction. Notably, Cu<sub>25</sub>Zn-A shows negligible Raman peaks of Zn-OH and CO<sub>3</sub><sup>2-</sup> for Zn<sub>5</sub>(CO<sub>3</sub>)<sub>2</sub>(OH)<sub>6</sub> compared with Zn-A in the in-situ Raman spectra at 5 mA cm<sup>-2</sup> (Figure S12). Therefore, Zn<sub>5</sub>(CO<sub>3</sub>)<sub>2</sub>(OH)<sub>6</sub> and Zn(OH)<sub>2</sub> are much easier to be formed on Zn-A than those on Cu<sub>25</sub>Zn-A, that is, the Cu-incorporation can prevent the surface from poisoning effectively.

The XPS survey spectrum verifies that Cu<sub>25</sub>Zn-A is consisted by Zn, O and Cu (Figure S13a). The Cu 2p XPS spectrum shows that Cu<sup>+</sup> is dominant in Cu<sub>25</sub>Zn-A (Inset in Fig. 3c) [33,34]. Additionally, the XPS Auger Cu LMM spectrum further confirms Cu<sup>+</sup> in Cu<sub>25</sub>Zn-A (Figure S13b), which may play the dominant role in the reduction of CO<sub>2</sub> [35,36]. The O 1 s XPS spectra show the existence of adsorbed water, metal-OH and metal-O signals, corresponding to chemically adsorbed water, hydrated metal oxide and metal oxide (Figure S13c). Importantly, the Zn 2p XPS spectra show that Zn in Cu<sub>25</sub>Zn-A is corresponding to Zn<sup>2+</sup> of ZnO, and that in Zn-A is related to Zn<sup>2+</sup> of Zn(OH)<sub>2</sub> or Zn<sub>5</sub>(CO<sub>3</sub>)<sub>2</sub>(OH)<sub>6</sub> (Fig. 3c) [30,33,34,37,38], consistent with the XRD and Raman results.

High-resolution TEM (HRTEM) images of Cu<sub>25</sub>Zn-A show the continuous crystal lattice fringes with the spacings of 0.15, 0.19 and 0.24 nm, which are coincident with ZnO (100), ZnO (101) and ZnO (102), respectively (Fig. 3d-e). ZnO (100) (0.28 nm) and ZnO (101) (0.24 nm) are observed in the HRTEM images of Zn-A. Importantly, we can also see the crystal lattice fringes with the spacings of 0.35 and 0.32 nm in Zn-A, which are related to Zn(OH)<sub>2</sub> (111) and

Zn<sub>5</sub>(CO<sub>3</sub>)<sub>2</sub>(OH)<sub>6</sub> (020), respectively. Therefore, Zn(OH)<sub>2</sub> and Zn<sub>5</sub>(CO<sub>3</sub>)<sub>2</sub>(OH)<sub>6</sub> are formed and embedded in the ZnO microstructure of Zn-A during the CO<sub>2</sub> reduction (Fig. 3d). However, only ZnO phase can be observed in the HRTEM images of Cu<sub>25</sub>Zn-A, indicating the Cu-incorporation could prevent Zn(OH)<sub>2</sub> and Zn<sub>5</sub>(CO<sub>3</sub>)<sub>2</sub>(OH)<sub>6</sub> from forming (Fig. 3e).

Our systematical characterizations show that the OH<sup>-</sup> and CO<sub>3</sub><sup>2-</sup> in the electrolyte react with Zn<sup>2+</sup> on the surface of Zn-A during the e-CO<sub>2</sub>RR process, leading to surface poisoning by forming Zn(OH)<sub>2</sub> and Zn<sub>5</sub>(CO<sub>3</sub>)<sub>2</sub>(OH)<sub>6</sub>, which cover the active sites on the surface and hamper the CO<sub>2</sub> reduction. On the contrary, their formations on Cu<sub>25</sub>Zn-A are effectively avoided, resulting in the anti-poisoning surface.

### 3.3. Surface state evolution

As we know, the surface reconstruction plays crucial roles in the electrocatalytic processes. Here we used the EDS in SEM, XPS and ex-situ Raman spectra to study the surface structure before and after e-CO<sub>2</sub>RR. The SEM images and EDS show that the surface morphology and elemental concentrations of Cu<sub>25</sub>Zn-A change after e-CO<sub>2</sub>RR (Fig. 2a, S3, S8 & S14). The Zn 2p XPS spectra of Cu<sub>25</sub>Zn-A before e-CO<sub>2</sub>RR showed that Zn is attributed to Zn<sup>2+</sup> in ZnO (Figure S15a) [38]. The Cu 2p XPS spectra showed that Cu is attributed to Cu<sup>2+</sup> mainly before e-CO<sub>2</sub>RR [39], which is higher than that after e-CO<sub>2</sub>RR, suggesting that Cu is reduced in the e-CO<sub>2</sub>RR (Figure S15b). The Raman spectra shows that the intensities of Zn-O peaks are reduced after e-CO<sub>2</sub>RR, and the peaks for Cu-O are strong, indicating that the surface of Cu<sub>25</sub>Zn-A is enriched with Cu oxides (Figure S16). The electronic resonance spectroscopy

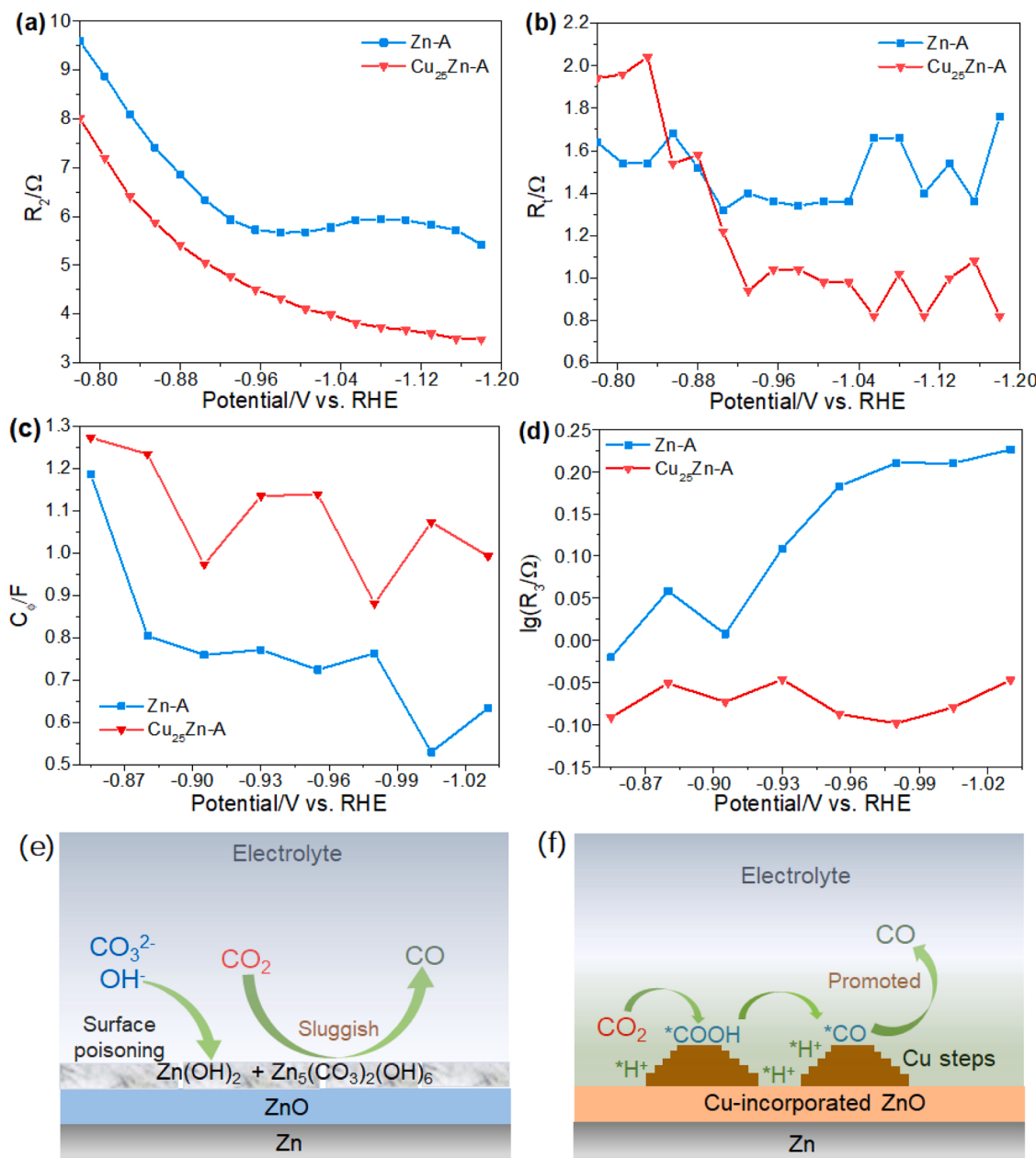


**Fig. 5.** (a) Plots of charge transfer resistance-potential and (b) Plots of mass diffusion resistance-potential at low of Nyquist plot. (c) Plots of  $C_{\phi}$ -potential and (d) Plots of  $\lg(R_3)$ -potential of Cu<sub>25</sub>Zn-A and Zn-A. (e) Scheme of e-CO<sub>2</sub>RR and surface poisoning on Zn-A and (f) mechanism of e-CO<sub>2</sub>RR on Cu<sub>25</sub>Zn-A.

(ESR) spectra show that the intensity of ESR peak at  $B = 330$  mT increase obviously after e-CO<sub>2</sub>RR, indicating that the amount of defects in Cu<sub>25</sub>Zn-A increases (Figure S17) [40].

The surface evolution can be illustrated by in-situ Raman scattering further. Starting from the as-prepared Cu<sub>25</sub>Zn-A, the peak intensities for both Zn-O and Cu-O become weaker and disappear gradually from the open circuit potential (OCP) to 5 mA cm<sup>-2</sup>, suggesting that the in-situ generated metallic phase is present on the surface of Cu<sub>25</sub>Zn-A in the e-CO<sub>2</sub>RR process (Fig. 4a) [41]. After returning to OCP, the Zn-O and Cu-O peaks gradually appear, indicating the in-situ generated metallic phases are re-oxidized [42,43]. Notably, the intensity of Cu-O is higher than that of Zn-O, suggesting that the Cu ions segregate on the surface in the reconstruction process, and the in-situ generated metallic phase should be Cu-enriched (Fig. 4a).

It has been reported that the step sites of Cu can promote the e-CO<sub>2</sub>RR [44], which can be determined by the \*CO binding modes [45]. For the Cu<sub>25</sub>Zn-A, the obvious peaks at  $\sim 1950$  cm<sup>-1</sup> and  $\sim 2080$  cm<sup>-1</sup>

are observed when the current density is up to 4 and 5 mA cm<sup>-2</sup>, which are attributed to the \*CO molecules adsorbed on the in-situ generated Cu steps [46]. Notably, the in-situ Raman spectra of Zn-A in a range of 1800–3000 cm<sup>-1</sup> shows negligible peak (Figure S18). Therefore, we can infer that the Cu steps are formed during the e-CO<sub>2</sub>RR process (Fig. 4b) [45]. The quasi in-situ ESR was utilized to study the defect in electrocatalyst, which can be formed in the e-CO<sub>2</sub>RR process. We can see that there is no obvious ESR peak for metal Zn, and the Cu-A measured at the 5<sup>th</sup> minute after the 1 h stability test. Meanwhile, the Zn-A and Cu<sub>25</sub>Zn-A measured at the 5<sup>th</sup> minute after the 1 h stability test shows obvious ESR peak at  $B = 330$  mT. Notably, the intensities of the ESR peaks for Cu<sub>25</sub>Zn-A are much stronger than those Zn-A measured at the 5<sup>th</sup> minute after the stability test. The above ESR results show that the defects are in Zn oxide mainly, and the Cu-incorporation can enhance the density of defects in Zn oxide (Fig. 4c) [47–49].

The ex-/in-situ Raman and quasi in-situ ESR spectroscopies demonstrate that the metallic Cu phase and defects are formed on Cu<sub>25</sub>Zn-A

during the reduction process, which shall result in: (1) hampering the  $\text{CO}_3^{2-}/\text{OH}^-$  adsorption for the surface anti-poisoning, and (2) facilitating the adsorption/activation of reactants and stabilization of intermediates [38]. The process of surface reconstruction on  $\text{Cu}_{25}\text{Zn-A}$  in e- $\text{CO}_2\text{RR}$  is illustrated in Fig. 4d.

### 3.4. Mechanism of e- $\text{CO}_2\text{RR}$ improvement

It is well-known that the  $\text{CO}_2$ -to-CO conversion process includes four basic steps (1–4) (\* represents adsorption states) [50]:



The operando EIS was done to study the promotion mechanism for each step. The charge and mass transports on the surface of electrocatalyst can be characterized by the Nyquist plots. The large radius of Nyquist plot in high frequency zone represents the charge transfer resistance ( $R_2$ ) [51] (Figure S19). The  $R_2$ -potential relationships show that  $\text{Cu}_{25}\text{Zn-A}$  has lower  $R_2$  value than Zn-A at the same potential due to the surface poisoning on Zn-A (Fig. 5a). Therefore, the charge transfer kinetics on  $\text{Cu}_{25}\text{Zn-A}$  is more beneficial. Additionally, the mass transfer resistance ( $R_t$ ) can be estimated from the Nyquist plot by measuring the small semicircle at high x-axis value interval (or called low frequency zone) [51].  $\text{Cu}_{25}\text{Zn-A}$  shows lower  $R_t$  value than Zn-A, especially when the potential (negative) is less than  $-0.88$  V, indicating the mass diffusion resistance of  $\text{Cu}_{25}\text{Zn-A}$  is smaller. As  $R_t$  is related to the resistance for the adsorption/desorption processes of reactants, intermediates and products, the small  $R_t$  results in the improved activity of  $\text{Cu}_{25}\text{Zn-A}$  in e- $\text{CO}_2\text{RR}$  (Fig. 5b).

The proton not only suppresses the formations of  $\text{Zn}(\text{OH})_2$  and  $\text{Zn}_5(\text{CO}_3)_2(\text{OH})_6$ , but also is the irreplaceable feedstock for the hydrogenation and deoxygenation in e- $\text{CO}_2\text{RR}$ . Therefore, the proton amount and transfer behavior on the surface are also important. Here, we use the second parallel components,  $C_\varphi$  and  $R_2$ , which are the pseudo capacitance and resistance for the surface hydrogen adsorption, respectively [52,53] (Figure S20 & Table S2), to evaluate the proton amount and transfer. At the same potential, we see that the  $C_\varphi$  value of  $\text{Cu}_{25}\text{Zn-A}$  is much larger than that of Zn-A, suggesting the highly accumulated protons on  $\text{Cu}_{25}\text{Zn-A}$  (Fig. 5c). Meanwhile, the  $\lg R_2$  values of  $\text{Cu}_{25}\text{Zn-A}$  are smaller than those of Zn-A, indicating the proton adsorption on  $\text{Cu}_{25}\text{Zn-A}$  is easy (Fig. 5c). Additionally, the mobility of adsorbed proton can also be quantified by the  $\lg R_2$  vs. potential plot [54]. Notably, the  $\lg R_2$  value increases as the potential decreases from  $-0.9$  to  $-1.0$  V for Zn-A, while that decreases for  $\text{Cu}_{25}\text{Zn-A}$  (Fig. 5d) [55], indicating the small proton adsorption resistance and fast proton transportation, which may benefit for the hydrogenation and deoxygenation steps of e- $\text{CO}_2\text{RR}$  [56,57]. Therefore, The Cu-incorporation not only achieve the surface anti-poisoning, but also enhance the proton amount and transportation on the surface of  $\text{Cu}_{25}\text{Zn-A}$ . The mechanism for the improved e- $\text{CO}_2\text{RR}$  is shown in Fig. 5(e-f).

## 4. Conclusion

In summary, we report Cu-incorporated  $\text{ZnO}$  on Zn plate for the effective reduction of  $\text{CO}_2$  to CO. We show that a CO FE > 90% and a CO partial current density of  $9.19 \text{ mA cm}^{-2}$  as well as a CO yield rate of  $0.49 \text{ mmol h}^{-1} \text{ cm}^{-2}$  are achieved on  $\text{Cu}_{25}\text{Zn-A}$  at  $-0.98$  V. The high e- $\text{CO}_2\text{RR}$  performance of  $\text{Cu}_{25}\text{Zn-A}$  is attributed to the weakened  $\text{CO}_3^{2-}/\text{OH}^-$  affinity on surface, hampering the formation of  $\text{Zn}_5(\text{CO}_3)_2(\text{OH})_6$  and  $\text{Zn}(\text{OH})_2$  and therefore preventing the surface from poisoning. Meanwhile, the reconstructed surface with stepped metallic Cu sites improves

the reactants adsorption/activation and stabilizes the intermediates. Moreover, the synergistic effect between Cu and Zn oxide improves the deoxygenation step and promotes the  $\text{CO}_2$ -to-CO conversion too. Our work may provide insightful understanding on the mechanism and guide the design of novel electrocatalyst for effective electrochemical  $\text{CO}_2$  reduction.

## CRediT authorship contribution statement

**Jinxian Feng:** Methodology, Investigation, Data curation, Formal analysis, Writing – original draft. **Junyan Li:** Data curation. **Lulu Qiao:** Data curation, Writing – review & editing. **Dong Liu:** Data curation. **Pengfei Zhou:** Data curation, Writing – review & editing. **Jun Ni:** Writing – review & editing, Funding acquisition. **Hui Pan:** Conceptualization, Visualization, Writing – review & editing, Supervision, Project administration, Funding acquisition.

## Declaration of Competing Interest

The authors declare that they have no known competing financial interests or personal relationships that could have appeared to influence the work reported in this paper.

## Data Availability

Data will be made available on request.

## Acknowledgements

This work was supported by the Science and Technology Development Fund (FDCT) from Macau SAR (0081/2019/AMJ, 0154/2019/A3, 0033/2019/AMJ, 0111/2022/A2, and 006/2022/ALC), Multi-Year Research Grants (MYRG2020-00026-FST and MYRG2022-00026-IAPME) from Research & Development Office at University of Macau, and Shenzhen-Hong Kong-Macao Science and Technology Research Programme (Type C) (SGDX20210823103803017) from Shenzhen. Jun Ni is thankful for the support of the National Natural Science Foundation of China (No. 22078301 and 21875220).

## Appendix A. Supporting information

Supplementary data associated with this article can be found in the online version at doi:10.1016/j.apcatb.2023.122665.

## References

- [1] Y. Yuan, Q. Wang, Y. Qiao, X. Chen, Z. Yang, W. Lai, T. Chen, G. Zhang, H. Duan, M. Liu, H. Huang, In situ structural reconstruction to generate the active sites for  $\text{CO}_2$  electroreduction on bismuth ultrathin nanosheets, *Adv. Energy Mater.* 12 (2022), 2200970, <https://doi.org/10.1002/aenm.202200970>.
- [2] J. Feng, J. Ni, H. Pan, Synergistic carbon and hydrogen reactions in the electrochemical reduction of  $\text{CO}_2$  to liquid fuels, *J. Mater. Chem. A* 9 (2021) 10546–10561, <https://doi.org/10.1039/dta00758k>.
- [3] A.A. Al-Absi, M. Mohamedali, A. Domin, A.M. Benneker, N. Mahinpey, Development of in situ polymerized amines into mesoporous silica for direct air  $\text{CO}_2$  capture, *Chem. Eng. J.* 447 (2022), 137465, <https://doi.org/10.1016/j.cej.2022.137465>.
- [4] R. Wu, D. Liu, J. Geng, H. Bai, F. Li, P. Zhou, H. Pan, Electrochemical reduction of  $\text{CO}_2$  on single-atom catalysts anchored on N-terminated TiN (111): low overpotential and high selectivity, *Appl. Surf. Sci.* 602 (2022), 154239, <https://doi.org/10.1016/j.apsusc.2022.154239>.
- [5] T. Dou, Y. Qin, F. Zhang, X. Lei, CuS nanosheet arrays for electrochemical  $\text{CO}_2$  reduction with surface reconstruction and the effect on selective formation of formate, *ACS Appl. Energy Mater.* 4 (2021) 4376–4384, <https://doi.org/10.1021/acsaem.0c03190>.
- [6] Y.J. Ko, J.Y. Kim, W.H. Lee, M.G. Kim, T.Y. Seong, J. Park, Y. Jeong, B.K. Min, W. S. Lee, D.K. Lee, H.S. Oh, Exploring dopant effects in stannic oxide nanoparticles for  $\text{CO}_2$  electro-reduction to formate, *Nat. Commun.* 13 (2022) 2205, <https://doi.org/10.1038/s41467-022-29783-7>.
- [7] B. Ren, G. Wen, R. Gao, D. Luo, Z. Zhang, W. Qiu, Q. Ma, X. Wang, Y. Cui, L. Ricardez-Sandoval, A. Yu, Z. Chen, Nano-crumples induced Sn-Bi bimetallic interface pattern with moderate electron bank for highly efficient  $\text{CO}_2$

electroreduction, *Nat. Commun.* 13 (2022) 2486, <https://doi.org/10.1038/s41467-022-29861-w>.

[8] G. Wu, Y. Song, Q. Zheng, C. Long, T. Fan, Z. Yang, X. Huang, Q. Li, Y. Sun, L. Zuo, S. Lei, Z. Tang, Selective electroreduction of CO<sub>2</sub> to n-propanol in two-step tandem catalytic system, *Adv. Energy Mater.* (2022), 2202054, <https://doi.org/10.1002/aenm.202202054>.

[9] L. Ji, L. Chang, Y. Zhang, S. Mou, T. Wang, Y. Luo, Z. Wang, X. Sun, Electrocatalytic CO<sub>2</sub> reduction to alcohols with high selectivity over a two-dimensional Fe<sub>2</sub>P<sub>2</sub>S<sub>6</sub> nanosheet, *ACS Catal.* 9 (2019) 9721–9725, <https://doi.org/10.1021/acscatal.9b03180>.

[10] S. Lamaison, D. Wakerley, J. Blanchard, D. Montero, G. Rousse, D. Mercier, P. Marcus, D. Taverna, D. Giaume, V. Mougel, M. Fontecave, High-current-density CO<sub>2</sub>-to-CO electroreduction on Ag-alloyed Zn dendrites at elevated pressure, *Joule* 4 (2020) 395–406, <https://doi.org/10.1016/j.joule.2019.11.014>.

[11] Q. Lu, C. Chen, Q. Di, W. Liu, X. Sun, Y. Tuo, Y. Zhou, Y. Pan, X. Feng, L. Li, D. Chen, J. Zhang, Dual role of pyridinic-N doping in carbon-coated Ni nanoparticles for highly efficient electrochemical CO<sub>2</sub> reduction to CO over a wide potential range, *ACS Catal.* 12 (2022) 1364–1374, <https://doi.org/10.1021/acscatal.1c04825>.

[12] Y.-Y. Liu, H.-L. Zhu, Z.-H. Zhao, N.-Y. Huang, P.-Q. Liao, X.-M. Chen, Insight into the effect of the d-orbital energy of copper ions in metal-organic frameworks on the selectivity of electroreduction of CO<sub>2</sub> to CH<sub>4</sub>, *ACS Catal.* 12 (2022) 2749–2755, <https://doi.org/10.1021/acscatal.1c04805>.

[13] L. Zhang, X.X. Li, Z.L. Lang, Y. Liu, J. Liu, L. Yuan, W.Y. Lu, Y.S. Xia, L.Z. Dong, D. Q. Yuan, Y.Q. Lan, Enhanced cuprophilic interactions in crystalline catalysts facilitate the highly selective electroreduction of CO<sub>2</sub> to CH<sub>4</sub>, *J. Am. Chem. Soc.* 143 (2021) 3808–3816, <https://doi.org/10.1021/jacs.0c11450>.

[14] H.L. Zhu, H.Y. Chen, Y.X. Han, Z.H. Zhao, P.Q. Liao, X.M. Chen, A porous π-π stacking framework with dicopper(I) sites and adjacent proton relays for electroreduction of CO<sub>2</sub> to C<sub>2+</sub> products, *J. Am. Chem. Soc.* 144 (2022) 13319–13326, <https://doi.org/10.1021/jacs.2c04670>.

[15] B. Zhao, M. Sun, F. Chen, Y. Shi, Y. Yu, X. Li, B. Zhang, Unveiling the activity origin of iron nitride as catalytic material for efficient hydrogenation of CO<sub>2</sub> to C<sub>2+</sub> hydrocarbons, *Angew. Chem. Int. Ed.* 60 (2021) 4496–4500, <https://doi.org/10.1002/anie.202015017>.

[16] S. Sarp, S. Gonzalez Hernandez, C. Chen, S.W. Sheehan, Alcohol production from carbon dioxide: methanol as a fuel and chemical feedstock, *Joule* 5 (2021) 59–76, <https://doi.org/10.1016/j.joule.2020.11.005>.

[17] G. Wang, J. Chen, Y. Ding, P. Cai, L. Yi, Y. Li, C. Tu, Y. Hou, Z. Wen, L. Dai, Electrocatalysis for CO<sub>2</sub> conversion: from fundamentals to value-added products, *Chem. Soc. Rev.* 50 (2021) 4993–5061, <https://doi.org/10.1039/dcos00071j>.

[18] A. Botz, J. Clausmeyer, D. Ohl, T. Tarnev, D. Franzen, T. Turek, W. Schuhmann, Local activities of hydroxide and water determine the operation of silver-based oxygen depolarized cathodes, *Angew. Chem. Int. Ed.* 57 (2018) 12285–12289, <https://doi.org/10.1002/anie.201807798>.

[19] J.S. Derrick, M. Loipersberger, S.K. Nistanaki, A.V. Rothweiler, M. Head-Gordon, E. M. Nichols, C.J. Chang, Templatting bicarbonate in the second coordination sphere enhances electrochemical CO<sub>2</sub> reduction catalyzed by iron porphyrins, *J. Am. Chem. Soc.* 144 (2022) 11656–11663, <https://doi.org/10.1021/jacs.2c02972>.

[20] W. Zhu, L. Zhang, S. Liu, A. Li, X. Yuan, C. Hu, G. Zhang, W. Deng, K. Zang, J. Luo, Y. Zhu, M. Gu, Z.J. Zhao, J. Gong, Enhanced CO<sub>2</sub> electroreduction on neighboring Zn/Co monomers by electronic effect, *Angew. Chem. Int. Ed.* 59 (2020) 12664–12668, <https://doi.org/10.1002/anie.201916218>.

[21] W. Luo, J. Zhang, M. Li, A. Züttel, Boosting CO production in electrocatalytic CO<sub>2</sub> reduction on highly porous Zn catalysts, *ACS Catal.* 9 (2019) 3783–3791, <https://doi.org/10.1021/acscatal.8b05109>.

[22] J. Wang, G. Wang, J. Zhang, Y. Wang, H. Wu, X. Zheng, J. Ding, X. Han, Y. Deng, W. Hu, Inversely tuning the CO<sub>2</sub> electroreduction and hydrogen evolution activity on metal oxide via heteroatom doping, *Angew. Chem. Int. Ed.* 60 (2021) 7602–7606, <https://doi.org/10.1002/anie.202016022>.

[23] K. Malik, B.M. Rajbongshi, A. Verma, Syngas production from electrochemical reduction of CO<sub>2</sub> at high current density using oxide derived Zn/Cu nanocomposite, *J. CO<sub>2</sub> Util.* 33 (2019) 311–319, <https://doi.org/10.1016/j.jcou.2019.06.020>.

[24] Z. Zhang, G. Wen, D. Luo, B. Ren, Y. Zhu, R. Gao, H. Dou, G. Sun, M. Feng, Z. Bai, A. Yu, Z. Chen, "Two ships in a bottle" design for Zn-Ag-O catalyst enabling selective and long-lasting CO<sub>2</sub> electroreduction, *J. Am. Chem. Soc.* 143 (2021) 6855–6864, <https://doi.org/10.1021/jacs.0c12418>.

[25] A.H.M. da Silva, S.J. Raajman, C.S. Santana, J.M. Assaf, J.F. Gomes, M.T.M. Koper, Electrocatalytic CO<sub>2</sub> reduction to C<sub>2+</sub> products on Cu and Cu<sub>x</sub>Zn<sub>y</sub> electrodes: effects of chemical composition and surface morphology, *J. Electroanal. Chem.* 880 (2021), 114750, <https://doi.org/10.1016/j.jelechem.2020.114750>.

[26] P. Moreno-Garcia, N. Schlegel, A. Zanetti, A. Cedeno Lopez, M.J. Galvez-Vazquez, A. Dutta, M. Rahaman, P. Broekmann, Selective electrochemical reduction of CO<sub>2</sub> to CO on Zn-based foams produced by Cu<sup>2+</sup> and template-assisted electrodeposition, *ACS Appl. Mater. Interfaces* 10 (2018) 31355–31365, <https://doi.org/10.1021/acsami.8b09894>.

[27] Q. Huang, Y. Wang, B. Zhou, Y. Wei, F. Gao, T. Fujita, The effect of ZnAl-LDHs-CO<sub>3</sub> on the corrosion behaviour of Zn-5Al alloys in 3.5 wt% NaCl solution, *Corros. Sci.* 179 (2021), 109165, <https://doi.org/10.1016/j.corsci.2020.109165>.

[28] R. Cuscó, E. Alarcón-Lladó, J. Ibáñez, L. Artús, J. Jiménez, B. Wang, M.J. Callahan, Temperature dependence of Raman scattering in ZnO, *Phys. Rev. B* 75 (2007), <https://doi.org/10.1103/PhysRevB.75.165202>.

[29] Y. Zhao, X. Zu, R. Chen, X. Li, Y. Jiang, Z. Wang, S. Wang, Y. Wu, Y. Sun, Y. Xie, Industrial-current-density CO<sub>2</sub>-to-C<sub>2+</sub> electroreduction by anti-swelling anion-exchange ionomer-modified oxide-derived Cu nanosheets, *J. Am. Chem. Soc.* 144 (2022) 10446–10454, <https://doi.org/10.1021/jacs.2c02594>.

[30] J. Moghaddam, S.B. Ghaffari, R. Sarraf-Mamoory, S. Mollaesmail, The study on the crystallization conditions of Zn<sub>5</sub>(OH)<sub>6</sub>(CO<sub>3</sub>)<sub>2</sub> and its effect on precipitation of ZnO nanoparticles from purified zinc ammoniacal solution, *Synth. React. Inorg.* 44 (2014) 895–901, <https://doi.org/10.1080/15533174.2012.740738>.

[31] S. Zhu, H. Bao, H. Zhang, H. Fu, Q. Zhao, L. Zhou, Y. Li, W. Cai, Optimal excitation wavelength for surface-enhanced raman spectroscopy: the role of chemical interface damping, *J. Phys. Chem. Lett.* 12 (2021) 11014–11021, <https://doi.org/10.1021/acs.jpcllett.1c03535>.

[32] K.H. Yu, J.M. Rhee, Y. Lee, K. Lee, S.-C. Yu, Surface-enhanced raman scattering study of 4-biphenylcarboxylic acid, *Langmuir* 1 (2001) 52–55.

[33] J. Hu, Y. Li, Y. Zhen, M. Chen, H. Wan, In situ FTIR and ex situ XPS/HS-LEIS study of supported Cu/Al<sub>2</sub>O<sub>3</sub> and Cu/ZnO catalysts for CO<sub>2</sub> hydrogenation, *Chin. J. Catal.* 42 (2021) 367–375, [https://doi.org/10.1016/s1872-2067\(20\)63672-5](https://doi.org/10.1016/s1872-2067(20)63672-5).

[34] P. Jongnavakit, P. Amornpitokut, S. Suwanboon, N. Ndiege, Preparation and photocatalytic activity of Cu-doped ZnO thin films prepared by the sol-gel method, *Appl. Surf. Sci.* 258 (2012) 8192–8198, <https://doi.org/10.1016/j.apsusc.2012.05.021>.

[35] P. Liu, E.J. Hensen, Highly efficient and robust Au/MgCuCr<sub>2</sub>O<sub>4</sub> catalyst for gas-phase oxidation of ethanol to acetaldehyde, *J. Am. Chem. Soc.* 135 (2013) 14032–14035, <https://doi.org/10.1021/ja406820f>.

[36] H. Li, Z. Su, S. Hu, Y. Yan, Free-standing and flexible Cu/Cu<sub>2</sub>O/Cu heterojunction net: a novel material as cost-effective and easily recycled visible-light photocatalyst, *Appl. Catal. B Environ.* 207 (2017) 134–142, <https://doi.org/10.1016/j.apcatb.2017.02.013>.

[37] J. Winiarski, W. Tylus, K. Winiarska, I. Szczęgiel, B. Szczęgiel, XPS and FT-IR characterization of selected synthetic corrosion products of zinc expected in neutral environment containing chloride ions, *J. Spectro.* 2018 (2018) 1–14, <https://doi.org/10.1155/2018/2079278>.

[38] Z. Geng, X. Kong, W. Chen, H. Su, Y. Liu, F. Cai, G. Wang, J. Zeng, Oxygen Vacancies in ZnO Nanosheets Enhance CO<sub>2</sub> Electrochemical Reduction to, in: C. O. Angew (Ed.), *Chem. Int.*, 57, 2018, pp. 6054–6059, <https://doi.org/10.1002/anie.201711255>.

[39] Y. Gao, L. Zhang, A.J.F. van Hoof, E.J.M. Hensen, On the surface-dependent oxidation of Cu<sub>2</sub>O during CO oxidation: Cu<sup>2+</sup> is more active than Cu<sup>+</sup>, *Appl. Catal. A: Gen.* 602 (2020), 117712 <https://doi.org/10.1016/j.apcata.2020.117712>.

[40] S. Chen, A.M. Abdel-Mageed, C. Mochizuki, T. Ishida, T. Murayama, J. Rabeh, M. Parlinska-Wojtan, A. Brückner, B.R. Jürgen, Controlling the O-vacancy formation and performance of Au/ZnO catalysts in CO<sub>2</sub> reduction to methanol by the ZnO particle size, *ACS Catal.* 11 (2021) 9022–9033, <https://doi.org/10.1021/acscatal.1c01415>.

[41] Q. Lei, L. Huang, J. Yin, B. Davaasuren, Y. Yuan, X. Dong, Z.P. Wu, X. Wang, K. X. Yao, X. Lu, Y. Han, Structural evolution and strain generation of derived-Cu catalysts during CO<sub>2</sub> electroreduction, *Nat. Commun.* 13 (2022) 4857, <https://doi.org/10.1038/s41467-022-32601-9>.

[42] T.L. Chen, H.C. Chen, Y.P. Huang, S.C. Lin, C.H. Hou, H.Y. Tan, C.W. Tung, T. S. Chan, J.J. Shyue, H.M. Chen, In situ unraveling of the effect of the dynamic chemical state on selective CO<sub>2</sub> reduction upon zinc electrocatalysts, *Nanoscale* 12 (2020) 18013–18021, <https://doi.org/10.1039/dnrr03475d>.

[43] S. Gong, G. Zhu, R. Wang, F. Rao, X. Shi, J. Gao, Y. Huang, C. He, M. Hojaberdi, Synergistically boosting highly selective CO<sub>2</sub>-to-CO photoreduction over BiOCl nanosheets via in-situ formation of surface defects and non-precious metal nanoparticles, *Appl. Catal. B: Environ.* 297 (2021), 120413, <https://doi.org/10.1016/j.apcatb.2021.120413>.

[44] P. Iyengar, M.J. Kolb, J. Pankhurst, F. Calle-Vallejo, R. Buonsanti, Theory-guided enhancement of CO<sub>2</sub> reduction to ethanol on Ag–Cu tandem catalysts via particle-size effects, *ACS Catal.* 11 (2021) 13330–13336, <https://doi.org/10.1021/acscatal.1c03717>.

[45] Z.Z. Wu, X.L. Zhang, Z.Z. Niu, F.Y. Gao, P.P. Yang, L.P. Chi, L. Shi, W.S. Wei, R. Liu, Z. Chen, S. Hu, X. Zheng, M.R. Gao, Identification of Cu(100)/Cu(111) interfaces as superior active sites for CO dimerization during CO<sub>2</sub> electroreduction, *J. Am. Chem. Soc.* 144 (2022) 259–269, <https://doi.org/10.1021/jacs.1c09508>.

[46] J. Gao, H. Zhang, X. Guo, J. Luo, S.M. Zakeeruddin, D. Ren, M. Gratzel, Selective C-C coupling in carbon dioxide electroreduction via efficient spillover of intermediates as supported by operando raman spectroscopy, *J. Am. Chem. Soc.* 141 (2019) 18704–18714, <https://doi.org/10.1021/jacs.9b07415>.

[47] A.J. Reddy, M.K. Kokila, H. Nagabushana, R.P.S. Chakradhar, C. Shivakumara, J. L. Rao, B.M. Nagabushana, Structural, optical and EPR studies on ZnO:Cu nanopowders prepared via low temperature solution combustion synthesis, *J. Alloy. Compd.* 509 (2011) 5349–5355, <https://doi.org/10.1016/j.jallcom.2011.02.043>.

[48] H. Hengming, S. Hui, K. Jiahui, L. Chunhua, Y. Jinhua, Atomic-level insights into surface engineering of semiconductors for photocatalytic CO<sub>2</sub> reduction, *J. Energy Chem.* 67 (2022) 309–341, <https://doi.org/10.1016/j.jechem.2021.10.015>.

[49] L. Zhang, Z. Li, X.-H. Zhang, C.-Y. Xu, Y.-W. Zhang, Elaborated reaction pathway of photothermal catalytic CO<sub>2</sub> conversion with H<sub>2</sub>-defective, *Surf. Chem. Eur. J.* 28 (2022), e202104490, <https://doi.org/10.1002/chem.202104490>.

[50] W. Liu, S. Wei, P. Bai, C. Yang, L. Xu, Robust coal matrix intensifies electron/substrate interaction of nickel-nitrogen (Ni-N) active sites for efficient CO<sub>2</sub> electroreduction at industrial current density, *Appl. Catal. B: Environ.* 299 (2021), 120661, <https://doi.org/10.1016/j.apcatb.2021.120661>.

[51] F. Bienen, D. Kopljær, A. Löwe, S. Geiger, N. Wagner, E. Klemm, K.A. Friedrich, Revealing mechanistic processes in gas-diffusion electrodes during CO<sub>2</sub> reduction via impedance spectroscopy, *ACS Sustainable Chem. Eng.* 8 (2020) 13759–13768, <https://doi.org/10.1021/acssuschemeng.0c04451>.

[52] L. Liao, S. Wang, J. Xiao, X. Bian, Y. Zhang, M.D. Scanlon, X. Hu, Y. Tang, B. Liu, H. H. Girault, A nanoporous molybdenum carbide nanowire as an electrocatalyst for hydrogen evolution reaction, *Energy Environ. Sci.* 7 (2014) 387–392, <https://doi.org/10.1039/c3ee42441c>.

[53] J. Li, H.-X. Liu, W. Gou, M. Zhang, Z. Xia, S. Zhang, C.-R. Chang, Y. Ma, Y. Qu, Ethylene-glycol ligand environment facilitates highly efficient hydrogen evolution of Pt/CoP through proton concentration and hydrogen spillover, *Energ. Environ. Sci.* 12 (2019) 2298–2304, <https://doi.org/10.1039/c9ee00752k>.

[54] J. Dai, Y. Zhu, Y. Chen, X. Wen, M. Long, X. Wu, Z. Hu, D. Guan, X. Wang, C. Zhou, Q. Lin, Y. Sun, S.C. Weng, H. Wang, W. Zhou, Z. Shao, Hydrogen spillover in complex oxide multifunctional sites improves acidic hydrogen evolution electrocatalysis, *Nat. Commun.* 13 (2022) 1189, <https://doi.org/10.1038/s41467-022-28843-2>.

[55] J. Li, J. Hu, M. Zhang, W. Gou, S. Zhang, Z. Chen, Y. Qu, Y. Ma, A fundamental viewpoint on the hydrogen spillover phenomenon of electrocatalytic hydrogen evolution, *Nat. Commun.* 12 (2021) 3502, <https://doi.org/10.1038/s41467-021-23750-4>.

[56] Z. Zhang, L. Bian, H. Tian, Y. Liu, Y. Bando, Y. Yamauchi, Z.L. Wang, Tailoring the surface and interface structures of copper-based catalysts for electrochemical reduction of CO<sub>2</sub> to ethylene and ethanol, *Small* 18 (2022), e2107450, <https://doi.org/10.1002/smll.202107450>.

[57] H. Ge, Y. Kuwahara, K. Kusu, H. Yamashita, Plasmon-induced catalytic CO<sub>2</sub> hydrogenation by a nano-sheet Pt/H<sub>x</sub>MoO<sub>3-y</sub> hybrid with abundant surface oxygen vacancies, *J. Mater. Chem. A* 9 (2021) 13898–13907, <https://doi.org/10.1039/d1ta02277f>.